Track Evaluation of GSM based Passive Radar: Model vs. Real-World Results

Sebastian Thomas Handke, Martina Broetje, Christian Steffes, Wolfgang Koch
Dept. Sensor Data and Information Fusion
Fraunhofer Institute for Communication, Information Processing and Ergonomics FKIE
Wachtberg, Germany
{sebastian.thomas.handke, martina.broetje, christian.steffes, wolfgang.koch}@fkie.fraunhofer.de

***Abstract*—Closing the feedback loop has proven essential for performance improvement and enhancing system reliability in a number of applications. Track evaluation addresses these goals by investigating system influences and analyzing discrepancies between expected and actual operation. Developing a model of a passive radar system which approximates its operational capabilities is therefore not only essential for performance prediction and pre-operational analysis but offers the opportunity for further system improvement. In the following, we assess the fit of a passive radar model to real-world data to investigate if it provides a reasonable representation of the observed results. There, we show that the detection probability model as well as the estimated lower bound on achievable estimation accuracy, where we utilize the Cramér-Rao Lower Bound (CRLB), give a reasonable approximation of real-world results collected by a passive radar system which utilizes Global System for Mobile Communications (GSM) signals.**

***Index Terms*—Track evaluation, passive radar, multistatic radar, mobile communication based PCL, Cramér-Rao lower bound, performance prediction**

I. Introduction

Passive radar systems utilize non-cooperative sources of illumination such as commercial broadcast and communication signals for target tracking, [1, 2]. From system constraints on each receiver up to the geometric layout of the full multistatic system, each factor has significant influence on the achievable estimation accuracy, [3, 4].

Track evaluation gives the opportunity to investigate these influences and analyze discrepancies between the model of a passive coherent localization (PCL) system and true system performance during operation. Depending on the quality of the model, such an assessment further provides the chance to reason about different aspects prior to operation with the goal to predict system performance. Track evaluation can therefore close the feedback loop and provide insights to facilitate further performance improvement and system reliability.

To evaluate and thereby optimize a software component within a real system, it is crucial to consider the entire processing chain of signal processing and target tracking while simultaneously taking geometrical and geographical influences into account that may impact the system. By comprehensively understanding and explaining these effects, we can acquire knowledge that assists our software development process.

A series of publications investigate optimal performance and operation criteria of passive radar systems such as [1, 2] where a number of them employ the CRLB as a metric [3, 4]. In the context of GSM based passive radar [5] considered operation criteria such as detection probability and visibility constraints, which was further extended in [6] as well as [7] presenting performance prediction and measurement evaluation of a GSM based PCL system utilizing the CRLB. Thereafter, [8] gave an evaluation of GSM passive radar data by investigating sensor parameter estimation techniques, a comparison of target detections with detection probabilities and the evaluation of different tracking configurations. While [9] examined further use cases of a mobile communication based PCL system, we presented in [10] an Evolutionary Algorithm to determine an optimal layout with regard to target state estimation based on the PCL model proposed in [6].

In the following, we evaluate the model's fit to real-world data to investigate if it provides a reasonable representation of real-world results. We present an in depth comparison of the model with results from a measurement campaign where we employed a GSM based passive radar system to track sea vessels in the Bay of Eckernförde, Germany. In this context, the employed detection probability model is compared to detections of each illuminator receiver pair and the estimated lower bound is set in relation to the achieved tracking error. We highlight geometric and geographical influences as well as discrepancies between the model and the achieved system performance.

After stating the necessary fundamentals in Sec. II and Sec. III, as well as the modeling assumptions in Sec. IV and Sec. V, which were previously also given in [10], we provide a brief overview of the applied passive radar tracking algorithm in Sec. VI. Sec. VII gives an in depth comparison, where, after describing the scenario in Sec. VII-A, we compare the detection probability model in Sec. VII-B and the estimated lower bound with real-world results in Sec. VII-C.

II. Bistatic Measurement Model

In a bistatic radar system a receiver (Rx) at position $\boldsymbol{o} = (o_x, o_y, o_z)^T$ receives the emitted signal from transmitter (Tx) at $\boldsymbol{s} = (s_x, s_y, s_z)^T$ both directly, and as a reflection off the target at $\boldsymbol{q} = (x, y, z)^T$. By correlating both signals, the target state parameters are estimated.

The bistatic range equation in Cartesian coordinates can be

written as $r = r_r + r_t = \| \boldsymbol{q} - \boldsymbol{o} \| + \| \boldsymbol{q} - \boldsymbol{s} \|$. The bistatic range-rate equation, as stated in [11], is given by

$$\dot{r} = -\lambda f_d = \left\langle \left[\frac{\boldsymbol{q}-\boldsymbol{o}}{\| \boldsymbol{q}-\boldsymbol{o} \|} + \frac{\boldsymbol{q}-\boldsymbol{s}}{\| \boldsymbol{q}-\boldsymbol{s} \|} \right], \boldsymbol{v} \right\rangle, \quad (1)$$

with wavelength λ, bistatic Doppler shift f_d, target velocity $\boldsymbol{v} = (\dot{x}, \dot{y}, \dot{z})^T$, and $\langle \cdot, \cdot \rangle$ corresponding to the dot product. The angle of the incoming echo in the x-y-plane of the receiver's field of view (FoV) can be calculated as $\varphi = \text{arctan2}(x - o_x, y - o_y) \in (-\pi, \pi]$, with arctan2$(\cdot)$ representing the four-quadrant inverse tangent. Therefore, the relationship of a target state $\boldsymbol{x} = (\boldsymbol{q}^T, \boldsymbol{v}^T)^T = (x, y, z, \dot{x}, \dot{y}, \dot{z})^T$ to a measurement in range, range-rate and azimuth is given by measurement equation $\boldsymbol{h}(\boldsymbol{x}, \boldsymbol{s}, \boldsymbol{o}) = (r, \dot{r}, \varphi)^T$.
Assuming an unbiased Gaussian distribution, a measurement $\boldsymbol{z}$ can be expressed as $\boldsymbol{z} = \boldsymbol{h}(\boldsymbol{x}, \boldsymbol{s}, \boldsymbol{o}) + \widetilde{\boldsymbol{v}}$, with $\widetilde{\boldsymbol{v}} \sim \mathcal{N}(\boldsymbol{0}, \boldsymbol{R})$, where $\mathcal{N}(\boldsymbol{0}, \boldsymbol{R})$ specifies a Gaussian distribution with zero mean and covariance matrix $\boldsymbol{R}$. We further assume $\boldsymbol{R}$ to be diagonal $\boldsymbol{R} = \text{diag}(\sigma_r^2, \sigma_{\dot{r}}^2, \sigma_\varphi^2)$ with variances $\sigma_r^2, \sigma_{\dot{r}}^2, \sigma_\varphi^2$.

III. Analysis of the Estimation Problem

Due to imprecise measurements, information from multiple Rx-Tx pairs have to be taken into account to achieve adequate target localization and tracking, [2]. The performance of a multistatic system can be analyzed by utilizing the Cramér-Rao Lower Bound (CRLB), which states that covariance matrix $\boldsymbol{C}$ of an unbiased estimator $\hat{\boldsymbol{x}}$ is bounded by the inverse of the Fisher information matrix (FIM) $\boldsymbol{J}(\hat{\boldsymbol{x}})$ [12]. Therefore, the multi-dimensional Cramér-Rao inequality is $\boldsymbol{C} \geq \boldsymbol{J}^{-1}(\hat{\boldsymbol{x}})$, compare [12], where matrix $\boldsymbol{J}^{-1}(\hat{\boldsymbol{x}})$ represents the CRLB.

A. CRLB under Assumption of Gaussian Noise

Following [6], the FIM $\boldsymbol{J}(\boldsymbol{x})$ for a Gaussian density $\boldsymbol{p}(\boldsymbol{z}|\boldsymbol{x}) = \mathcal{N}\big(\boldsymbol{z}; \boldsymbol{h}(\boldsymbol{x}), \mathbf{R}\big)$ with expectation $\boldsymbol{h}(\boldsymbol{x})$ and covariance $\mathbf{R}$, can be expressed as

$$\boldsymbol{J}(\boldsymbol{x}) = \frac{\partial \boldsymbol{h}(\boldsymbol{x})}{\partial \boldsymbol{x}}^T \mathbf{R}^{-1} \frac{\partial \boldsymbol{h}(\boldsymbol{x})}{\partial \boldsymbol{x}}. \quad (2)$$

For $N \in \mathbb{N}$ independent measurements $\boldsymbol{z}_i = \boldsymbol{h}_i(\boldsymbol{x}) + \widetilde{\boldsymbol{v}}_i$ with $\widetilde{\boldsymbol{v}}_i \sim \mathcal{N}(\boldsymbol{0}, \boldsymbol{R_i})$ where $i \in [1:N]$ and $\boldsymbol{h} = (\boldsymbol{h}_1, \ldots, \boldsymbol{h}_N)^T$,

$$\boldsymbol{J}(\boldsymbol{x}) = \sum_{i=1}^{N} \frac{\partial \boldsymbol{h}_i(\boldsymbol{x})}{\partial \boldsymbol{x}}^T \mathbf{R}_i^{-1} \frac{\partial \boldsymbol{h}_i(\boldsymbol{x})}{\partial \boldsymbol{x}} = \sum_{i=1}^{N} \boldsymbol{J}_i(\boldsymbol{x}). \quad (3)$$

Therefore, under the assumption of independent measurement error covariance matrices $\mathbf{R}_i$ the complete FIM $\boldsymbol{J}(\boldsymbol{x})$ can be stated as the sum over the corresponding FIMs $\boldsymbol{J}_i(\boldsymbol{x})$.

B. Incorporating Information Over Time

Via a suitable motion model, target measurements gathered at different instances in time can be incorporated into the estimation process, [6]. The transition equation for a deterministically moving target from time $\boldsymbol{t}_{k-1}$ to $\boldsymbol{t}_k$ can be stated as $\boldsymbol{x}_k = \mathbf{F}_{k|k-1} \boldsymbol{x}_{k-1}$ with transition matrix $\mathbf{F}_{k|k-1}$. Gathered measurement information over several scans lead to $\mathbf{J}(\boldsymbol{x}_k)$ at time $\boldsymbol{t}_k$ given by

$$\mathbf{J}(\boldsymbol{x}_k) = \sum_{s=1}^{k} \mathbf{F}_{k|s}^{-1T} \mathbf{J}(\boldsymbol{x}_s) \mathbf{F}_{k|s}^{-1}, \quad (4)$$

with $\mathbf{F}_{k|s}$ expressing the transition matrix from time $\boldsymbol{t}_s$ to $\boldsymbol{t}_k$, $s \leq k$. We assume the measurement noise to be constant over time in the following where $\boldsymbol{R}_s = \boldsymbol{R}\ \forall s \in \mathbb{N}$ and deterministic targets moving at constant velocity.

C. Root Cramér-Rao Lower Bound

To assess the expected estimation accuracy, we choose the root Cramér-Rao lower bound (RCRLB) which for example in x-y-position, where $\mathbf{J}^{-1}_{(1,1)}$ represents the entry of row one and column one in the CRLB matrix, can be expressed as

$$\text{RCRLB(x-y-position)} = \sqrt{\mathbf{J}^{-1}_{(1,1)}(\boldsymbol{x}) + \mathbf{J}^{-1}_{(2,2)}(\boldsymbol{x})}. \quad (5)$$

IV. Signal-to-noise Ratio

The SNR is calculated via the bistatic radar equation, compare [2], given by

$$\text{SNR}(r_t, r_r, w_{\phi_{T_x}} w_{\phi_{R_x}} \mathbf{1}_{\text{DEM}}) = \frac{P_{T_x} G_{R_x} G_{I_x} \sigma \lambda^2}{P_N (4\pi)^3 (r_t r_r)^2} w_{\phi_{T_x}} w_{\phi_{R_x}} \mathbf{1}_{\text{DEM}}, \quad (6)$$

with average transmit power P_{T_x} and average noise power $P_N = k_B T_0 B F$ defined as the product of Boltzmann constant k_B, system temperature T_0 in Kelvin, signal bandwidth B as well as noise factor F. The receiver antenna gain is described by G_{R_x}, the coherent signal integration gain by G_{I_x} and the target radar cross-section (RCS) by σ. Parameters $w_{\phi_{T_x}}$, $w_{\phi_{R_x}}$, and $\mathbf{1}_{\text{DEM}}$ entail signal propagation assumptions described subsequently.
The transmit power of a sector antenna typically decreases with increasing angle between the direction of the transmitted signal and its boresight [13]. To simplify this relationship, we partition the sector relative to the antenna boresight into several weighted angular segments. These are $[-180° : -120°), [-120° : -60°), [-60° : 60°], (60° : 120°], (120° : 180°)$ with respective weights $w_{\phi_{T_x}}$ of $0, 0.3, 1, 0.3, 0$.
We assume the receiver to be a uniform linear array (ULA) which can receive direct signals from any direction. Indirect signals reflected by the target are assumed to be receivable only in a sector of $[-60° : 60°]$ around its boresight accounted for by weight $w_{\phi_{R_x}}$ equal to 1 in the sector and 0 outside.
The receiver, transmitter, and target can be related in a digital elevation model (DEM) to identify locations where signals are shadowed by obstacles. Only for Rx-Tx pairs with an unobstructed line-of-sight (LoS) we assume reception of the direct signal. Similarly, we assume reception of target reflections only for Rx-Tx pairs with LoS to the target represented by indicator variable $\mathbf{1}_{\text{DEM}}$, which is equal to 1 if there is a LoS from Tx and Rx to the target and 0 otherwise. Other signal propagation effects are intentionally omitted in favor of a simplified binary shadowing model.

V. Information Reduction

Assuming a perfect sensor with detection probability P_D equal to one and false alarm probability P_F equal to zero is unrealistic for most real-world applications. Following [14], the effect of measurements with uncertain origin can be accounted for by multiplying the FIM with an information reduction factor. We compute this factor in form of the detection probability as the Swerling I model in conjunction with the minimum detectable velocity (MDV) model, compare [6, 15], given for a constant false alarm probability P_{FA} as

$$P_D(\mathrm{SNR}(\cdot), \dot{r}_k) = P_{FA}^{\frac{1}{1+\mathrm{SNR}(\cdot)}} \cdot \left(1 - \exp\left(-\ln(2)\left(\frac{\dot{r}_k}{\mathrm{MDV}}\right)^2\right)\right). \tag{7}$$

Please note, that choosing P_{FA} entails a general assumption on the magnitude of false alarms which we make in the P_D calculation. We do not model association uncertainties explicitly, since these are impacted by multiple factors of a real systems, such as a realistic structure of false alarms and the type of association procedure employed, which is out of the scope of this paper.

VI. Target tracking and fusion

A key role in passive radar is the sensor data fusion step. By combining different target, receiver, and transmitter geometries, it helps overcome the limitation in the accuracy of a single measurement and therefore leads to an improved position and velocity estimate, as well as enhanced detection capability for the whole system. During the last years, FKIE has developed a tracking architecture, based on multi hypothesis tracking (MHT), which has been tested with different passive radar transmitters [7, 16]. Here we apply a centralized fusion strategy, which sequentially updates the information from different transmitter and receiver pairs. Track extraction and termination is done according to the sequential likelihood testing, while the propagation model uses a nearly-constant velocity model.

VII. Real-World Data Comparison

In the following, the model is compared to data collected by a passive radar system of a ship target. After a brief description of the scenario, the estimated detection probability is first compared to the so-called mean number of detections and subsequently the tracking error is set in relation to the estimated RCRLB.

A. Scenario

The target, a ship with a length of less than $20\,\mathrm{m}$, travels on a long, elongated oval trajectory in the Bay of Eckernförde. Fig. 1 provides a scenario overview showing the terrain around the bay. The target starts near the shore and moves clockwise, first on the northern route before curving south and returning. Since it has sufficient distance to other targets during the scenario, we consider it to be an independent target.
The passive radar receiver is located on the shore near the

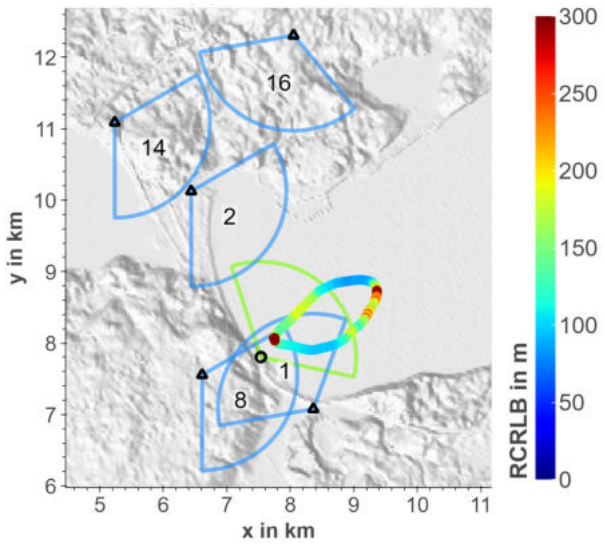

Fig. 1: Scenario overview: The receiver FoV is marked by a green sector, while each illuminator FoV is marked by a blue sector. The target trajectory is depicted as a colored line representing the RCRLB in x-y position given in [m].

P_{T_x}	40 dBm [18]	F_{dB}	8 dB	MDV	$5\,\mathrm{m\,s^{-1}}$
G_{R_x}	12 dB	T_0	300 K	σ_r	150 m
G_{I_x}	50 dB	B	200 kHz	$\sigma_{\mathrm{Doppler}}$	3 Hz
σ	$5\,\mathrm{m}^2$	P_{FA}	0.001	σ_φ	5°

TABLE I: Model parameters of the GSM-PCL scenario.

target's starting position and five suitable GSM illuminators around the bay were selected. In Fig. 1, each illuminator location and orientation is indicated by a black rectangle and a blue sector, respectively. The green sector indicates the receiver FoV and the black circle its position. The illuminators have the unique IDs 1, 2, 8, 14 and 16.
The cell site locations, heights above ground and boresight orientations of each antenna stem from [17]. The transmitting sector antenna heights range from $15\,\mathrm{m}$ to $32\,\mathrm{m}$ above ground, the GSM 900 receiver is at a height of approx. $11\,\mathrm{m}$ above ground. Further model parameters can be found in Tab. I. We assume a deterministic target moving with constant velocity. The Fisher information is computed with time difference Δt of $1\,\mathrm{s}$ between 10 consecutive updates, i.e. 11 time steps in total with the initial target state. Further, the Swerling I model in conjunction with the MDV model is employed to compute the detection probability.

B. Target Detections and Detection Probability Comparison

To set the detection probability model in relation to the target detections, we computed the so-called mean number of detections or mean detections. The target detections were generated as described in [8] and are given as Boolean values for each Rx-Tx-pair. Each blue line showing the mean number of detections in Fig. 3 is the result of applying an averaging window of length three to the Boolean detections. The estimated probability of detection (Pd) in Fig. 3 is given by a dashed black line. Fig. 3 shows the estimated detection

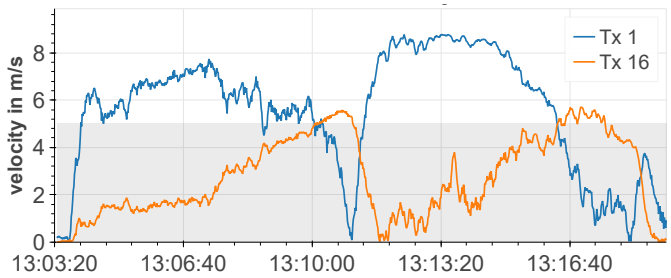

Fig. 2: Absolute value of the target's bistatic velocity with respect to Tx 1 and Tx 16. Velocities in the gray shaded area fall below the MDV.

probability and the mean number of detections for each Rx-Tx-pair, which we describe in the following in detail.

1) Tx 1: For Tx 1 in Fig. 3a, we observe that both curves reach a minimum at around 13:11, where the target turns. This can be attributed to a low bistatic velocity of the target during this maneuver. Fig. 2 shows the magnitude of the target's bistatic velocity along its trajectory with respect to Tx 1 as a blue curve where velocities below the MDV fall into the gray shaded area. There, the bistatic velocity of the target for Tx 1 falls towards zero at around 13:11. Correspondingly, the mean detections as well as the expected detection probability both drop to a minimum. Therefore, for this section the detection probability model reflects reality well.

Similarly, a low bistatic velocity with respect to Tx 1 can also be observed towards the end of the scenario. From approx. 13:16:20, the target's velocity falls below the MDV. This also leads to a decrease in detection probability, as seen in Fig. 3a. During this period, more detections are missing, which can be observed by intermittent drops in the blue curve in Fig. 3a. Although there are points in time where the target can be detected, there are still fewer detections during this period, indicating that the utilized model is appropriate.

Fig. 4a and Fig. 4d show a spatial comparison of the two quantities for Tx 1. There, the two regions where the target's velocity falls below the MDV are clearly visible.

In addition to the previously mentioned sections with low detection count, Fig. 4d also shows two more sections where detections are missing. One is halfway from the shore to the farthest point of the trajectory, and the other is halfway back on the southern section of the trajectory. These areas can be found in Fig. 3a from approx. 13:07:10 to 13:07:35 and from approx. 13:14:00 to 13:14:50. The cause for the lack of detections in the northern section cannot be determined definitively. The absence of detections in the southern section could be related to the illuminator's FoV and possible signal shadowing.

2) Tx 2: Fig. 3b shows a good match for the two quantities until 13:13:20. Thereafter, on the return along the southern section of the trajectory, two long sections stand out where the target is not detected, as shown in Fig. 4e. From 13:13:20 to approx. 13:14:45 and from approx. 13:15:20 to 13:16:50, detections are missing, even though the estimated detection probability, as indicated in Fig. 3b and Fig. 4b, suggests that

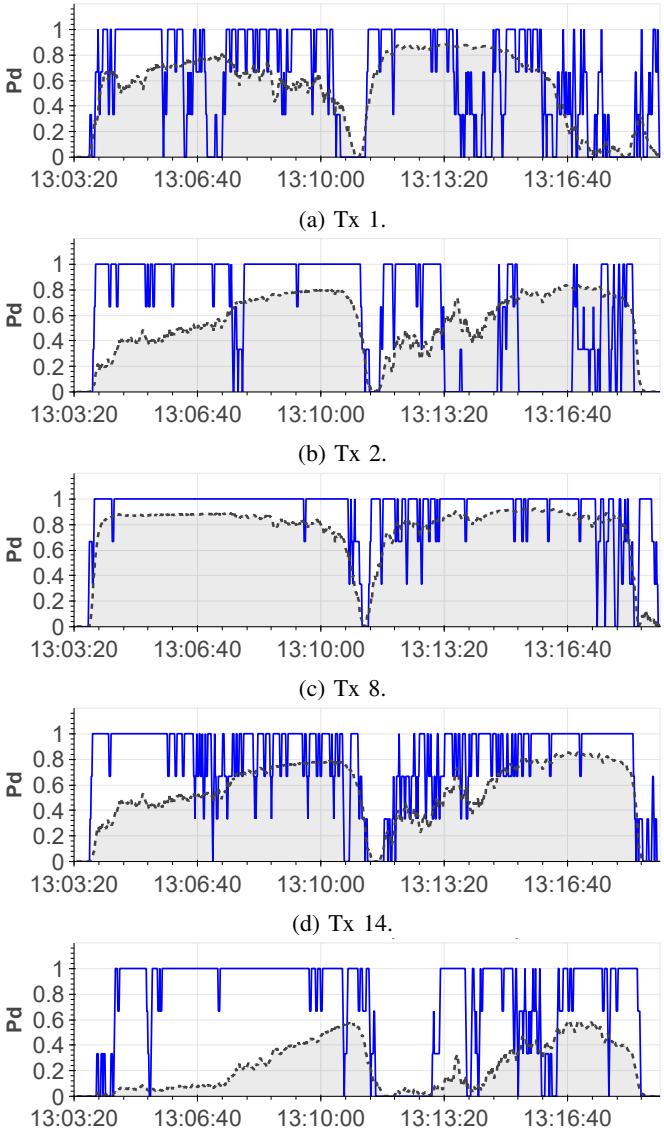

(a) Tx 1.

(b) Tx 2.

(c) Tx 8.

(d) Tx 14.

(e) Tx 16.

Fig. 3: The figure shows a comparison of the estimated detection probability (Pd), given as a black dashed line and the mean number of detections, given as a blue line.

the target should be detectable.

The reason for the absence of detections becomes evident when examining Fig. 5 which shows an azimuth-time-diagram with angular measurements marked as black asterisks of the relevant time span. For an angular range of approx. 75° to 100° appear repeatedly dark blue sections in Fig. 5, during which the cancellation of the direct signal seems to suppress too many signal components. Since for a successful target detection a range, Doppler and angular measurement all have to be available, missing the angular component leads to missing target detections during these sections.

3) Tx 8: In Fig. 3c, it is noticeable that both curves exhibit good agreement. At the time of the target's turning maneuver around 13:11, a decrease in both quantities can be observed.

The Doppler-time-diagram in Fig. 6 shows strong noise at

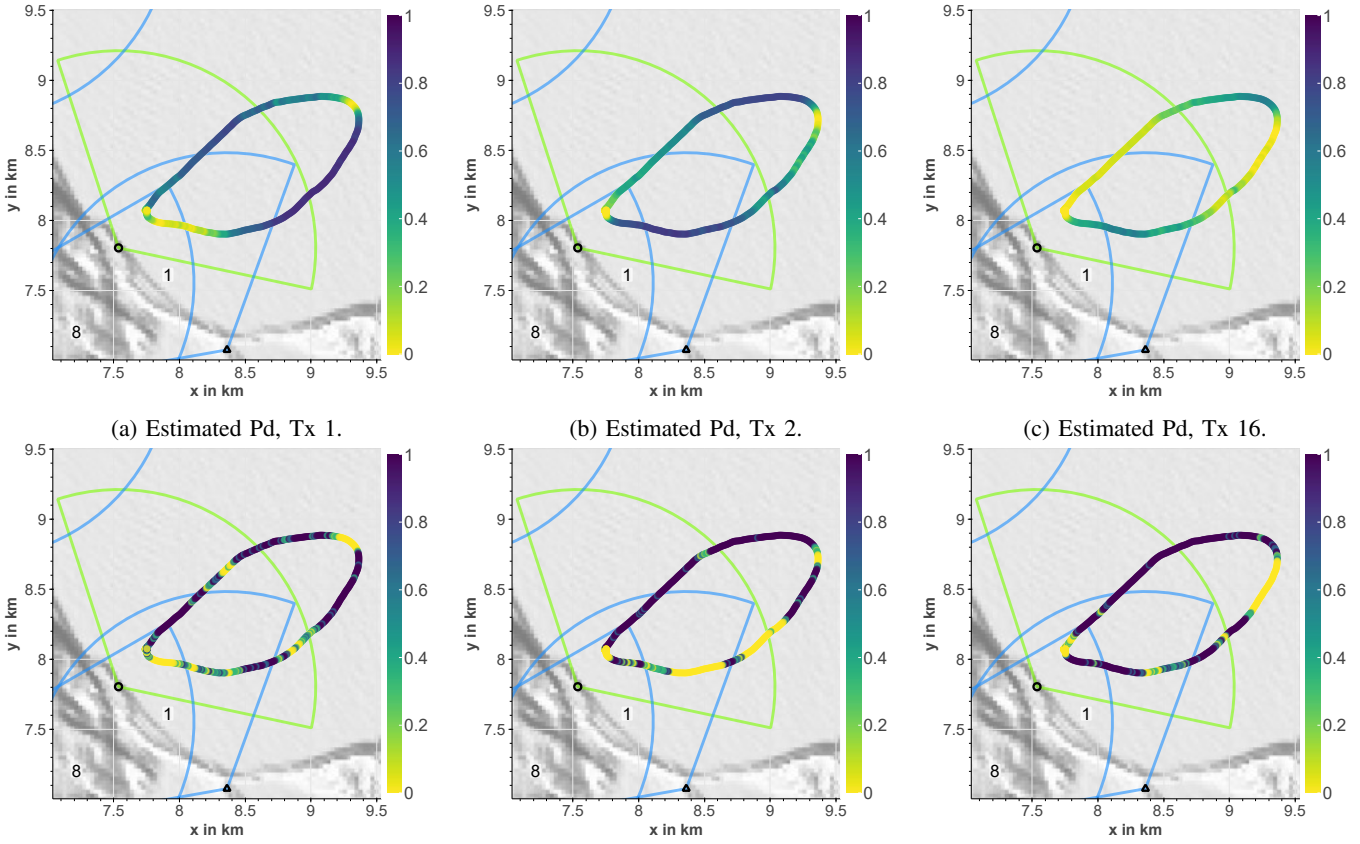

(a) Estimated Pd, Tx 1. (b) Estimated Pd, Tx 2. (c) Estimated Pd, Tx 16.

(d) Mean detections, Tx 1. (e) Mean detections, Tx 2. (f) Mean detections, Tx 16.

Fig. 4: Fig. 4a, Fig. 4b and Fig. 4c show the estimated detection probability along the trajectory for the respective illuminators Tx 1, Tx 2 and Tx 16 while Fig. 4d, Fig. 4e and Fig. 4f on the bottom row show the corresponding mean number of detections.

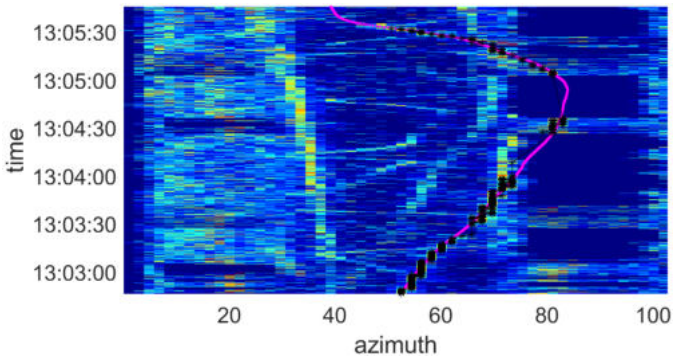

Fig. 5: The figure shows the azimuth-time-diagram with respect to Tx 2. The ground truth is shown as a pink line, target detections as black asterisks.

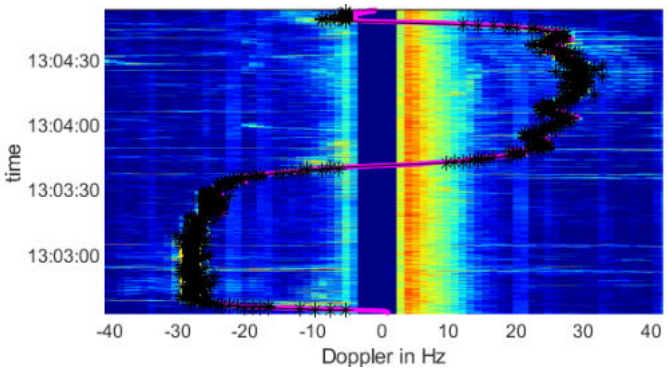

Fig. 6: The Doppler-time-diagram for Tx 8 shows the groundtruth as a pink line, target detections as black asterisks. The noise around 5 Hz, seen as a red area, can be attributed to wave motion.

a Doppler-frequency around 5 Hz for this illuminator. This noise can be attributed to wave motion, which leads to an asymmetric expansion of the clutter notch, compare [6, 15]. The intermittent absence of detections at the end of the trajectory can be related to this phenomenon.

4) Tx 14: The comparison for Tx 14 in Fig. 3d reveals again that the detection probability model fits the average number of detections.

5) Tx 16: Illuminator Tx 16 is the furthest away from the receiver. Fig. 3e shows the detection probability for this illuminator to be significantly lower compared to the ones previously presented. This can be attributed to the low bistatic target velocity depicted in Fig. 2 by the orange line which is mostly below the MDV.
Especially after the turning maneuver, the detection probability drops to a value close to zero, which is also reflected in the

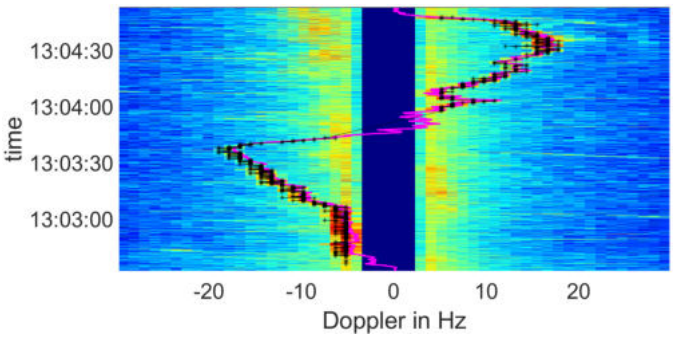

Fig. 7: The figure shows the Doppler-time-diagram for Tx 16. The ground truth is shown as a pink line, target detections as black asterisks.

missing detections. The agreement between the two quantities for this section can also be seen when comparing Fig. 4c and Fig. 4f.

When looking at the beginning of the trajectory, it is noticeable that the target can be detected, even though the detection probability is estimated to be low. The exact reason for the reliable detections in this section cannot be determined with certainty. On one hand a lower MDV of for example $3\,\mathrm{m\,s^{-1}}$ may lead to a more suitable detection probability result for this illuminator. On the other hand, the detections could be a random result.

When looking at the beginning of the trajectory in Fig. 7, it is noticeable that the target detections starting from approx. 13:04:30 until approx. 13:07:30 are close to the clutter notch around which signal noise may occur. However, for this section the signal is significantly stronger compared to subsequent sections, which indicates that the target detections are correct and therefore a reduction in MDV for this illuminator may be appropriate.

C. Estimated RCRLB and Tracking Error Comparison

In the following we present a comparison of the tracking error and the estimated RCRLB. Given the difficulty of modeling the generation process of real-world data and the unavailability to perform Monte Carlo runs in a realistic setup, an exact match between the two quantities is unlikely. The goal is therefore to investigate whether the presented model adequately reflects the trend of the tracking error and if plausible connections between the two quantities can be established. We found the CRLB to adequately model the trend of the real system and therefore decided not to use the more complex Posterior CRLB, see [19]. To account for motion uncertainties we compute the CRLB on a fixed time window, where the size of the time window models the temporal integration gain assumed.

To calculate the tracking error we perform the association of tracks and ground truth according to a distance metric in position and velocity coordinates. Using a time window, either the whole track or track segments are associated to account for diverging tracks or identity switches. Fig. 8a and Fig. 8b each show a comparison the two quantities for x-y-position and

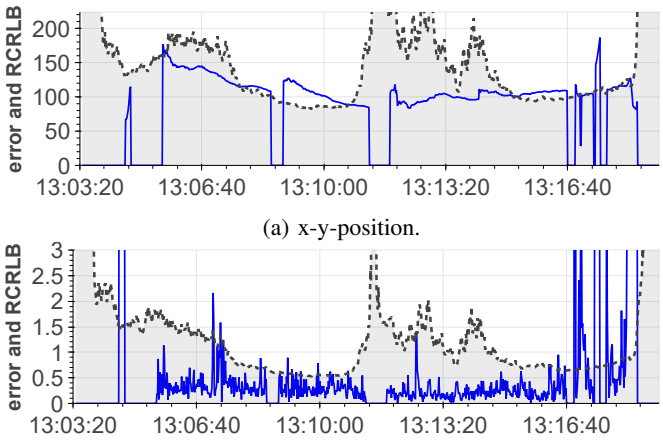

(a) x-y-position.

(b) x-y-velocity.

Fig. 8: Comparison of the tracking error, depicted by a blue line and the estimated RCRLB, depicted by a black dashed line with respect to x-y-position in Fig. 8a in $[\mathrm{m}]$ and x-y-velocity in Fig. 8b in $[\mathrm{m\,s^{-1}}]$.

x-y-velocity of the target. The tracking error is depicted by a blue line and the estimated RCRLB by a black dashed line. In case the tracking algorithm looses the target, no tracking error can be calculated and the blue line drops to zero.

Fig. 8a shows a very high RCRLB estimate with respect to the x-y-position in the beginning. For this section, the tracking algorithm is also unable to track the target. The target can only be tracked for a longer period starting at approx. 13:05:35. Initially, the RCRLB is significantly higher than the tracking error, indicating that the sensor may be more accurate for this section than assumed, before both quantities approach each other around 13:07:40. The tracking algorithm momentarily loses the target before being able to track it again with a higher error at around 13:08:55. The reason for the brief loss of the target cannot be determined conclusively. Around 13:11, during the turning maneuver, the RCRLB increases sharply, indicating a more challenging tracking configuration. The track is momentarily lost for this period before the target is found again at approx. 13:11:45. Subsequently, the tracking error remains below the estimated RCRLB for several minutes before they start to approach each other again. From around 13:15:20, both quantities follow a similar trend, with a minor outlier, until the RCRLB increases significantly at around 13:18:35, ultimately resulting in the loss of the target.

In summary, in this scenario, three track losses appear, the first one can not be explained by our model so further investigation is needed from the tracking side. This could for example involve to check if the tracker is associating correctly or gets confused by clutter measurements. The second loss is a combination of two effects. First, there is a strong maneuver, which suggests that the process model in tracking may not be adequate. Second, we are dealing with a more challenging measurement geometry, which amplifies the impact of the strong maneuver. The third loss can be explained by missing detections when the target stops. When comparing the tracking error and the RCRLB in x-y-velocity in Fig. 8b, it is noticeable

that the RCRLB in this component is estimated to be higher than the tracking error. At the beginning and end of the trajectory, there are some outliers in the tracking error, which can be attributed to the initialization of new tracks after the loss of the target. However, it is noticeable that an increase in the RCRLB in the x-y-velocity leads to a loss of the target both during the turning maneuver at around 13:11 and at the end of the trajectory, which can also be observed in a drop to zero in the blue curve. Similar increases can also be seen at the same time points in the x-y-position components. Since the estimated RCRLB is mostly higher than the tracking error, the sensor may be more accurate with regard to the velocity components than previously assumed.

VIII. Conclusion

The presented results show, that the passive radar model reflects the real-world data well in many respects. The detection probability model in form of the Swerling I model in conjunction with the MDV model fits reality to a significant degree.

The model provides the opportunity to assess the system for plausibility and identify discrepancies. As we saw for Tx 2, where due to the signal processing, the received signal from certain angular ranges was temporarily suppressed, leading to missed detections. This observation offers the potential to adjust the direct signal cancellation procedure.

Even though the tracking error and the estimated RCRLB do not match exactly in the presented target tracking context, it is possible to see plausible connections between the two quantities. Constellations where both variables complement each other are of particular interest, especially when increases in the estimated RCRLB relate to challenging tracking conditions. By observing the occurrence of track losses, it becomes evident how this tool can greatly assist in explaining situations and directing further investigations.

Regarding future work, there are a variety of perspectives. One would be to evaluate new scenarios involving alternative illuminators. Another is to improve the model and consequently its fit to real-world data.

IX. Acknowledgment

The authors would like to express their gratitude towards the "Wehrtechnische Dienststelle für Schiffe und Marinewaffen, Maritime Technologie und Forschung" (WTD 71) of the German Bundeswehr, which greatly supported this work.

This paper was reviewed and revised in parts with the assistance of ChatGPT by OpenAI for textual editing and grammatical support.

References

[1] H. Griffiths and C. Baker, "Passive coherent location radar systems. Part 1: Performance prediction," *IEEE Proceedings-Radar, Sonar and Navigation*, vol. 152, no. 3, pp. 153–159, 2005.

[2] N. J. Willis and H. D. Griffiths, *Advances in bistatic radar*. SciTech Publishing, 2007, vol. 2.

[3] M. Greco, P. Stinco, F. Gini, A. Farina, and M. Rangaswamy, "Cramér-Rao bounds and Tx-Rx selection in a multistatic radar scenario," in *2010 IEEE Radar Conference*. IEEE, 2010, pp. 1371–1376.

[4] M. S. Greco, P. Stinco, F. Gini, and A. Farina, "Cramér-Rao bounds and selection of bistatic channels for multistatic radar systems," *IEEE Transactions on Aerospace and Electronic Systems*, vol. 47, no. 4, pp. 2934–2948, 2011.

[5] U. R. O. Nickel, "System considerations for passive radar with GSM illuminators," in *2010 IEEE International Symposium on Phased Array Systems and Technology*, 2010, pp. 189–195.

[6] M. Brötje, *Multistatic multihypothesis tracking techniques for underwater and air surveillance applications*. GCA-Verlag, 2012.

[7] R. Zemmari, M. Broetje, G. Battistello, and U. Nickel, "GSM passive coherent location system: Performance prediction and measurement evaluation," *Radar, Sonar Navigation, IET*, vol. 8, no. 2, pp. 94–105, February 2014.

[8] Martina Broetje, Benjamin Knoedler, and Wolfgang Koch, *Evaluation of GSM Passive Radar Data and Its Use in Multistatic Tracking*. IEEE, 2016.

[9] C. Steffes, B. Demissie, B. Knoedler, M. Broetje, M. Mandt, and W. Koch, "Passive radar using mobile communication: A discussion of use cases and feasibility," in *2022 IEEE Radar Conference (RadarConf22)*, 2022, pp. 1–6.

[10] S. T. Handke, M. Broetje, C. Steffes, and W. Koch, "Mission planning for mobile communication passive radar via an evolutionary algorithm," in *2022 23rd International Radar Symposium (IRS)*. IEEE, 2022, pp. 338–343.

[11] N. J. Willis, *Bistatic radar*. SciTech Publishing, 2005, vol. 2.

[12] H. L. Van Trees, *Optimum array processing: Part IV of detection, estimation, and modulation theory*. John Wiley & Sons, 2004.

[13] J. H. Schiller, *Mobile communications*. Pearson education, 2003.

[14] T. Kirubarajan, H. Chen, and Y. Bar-Shalom, "Parameter estimation and the CRLB with uncertain origin measurements," *Methodology and Computing in Applied Probability*, vol. 3, no. 4, pp. 387–410, 2001.

[15] W. Koch, *Tracking and Sensor Data Fusion*, ser. Mathematical Engineering. Berlin, Heidelberg: Springer Berlin Heidelberg, 2014.

[16] M. Daun, U. Nickel, and W. Koch, "Tracking in multistatic passive radar systems using DAB/DVB-T illumination," *Signal Processing*, 2011.

[17] Bundesnetzagentur für Elektrizität, Gas, Telekommunikation, Post und Eisenbahnen (BNetzA), *Elektromagnetische Felder - EMF*, 2024, https://www.bundesnetzagentur.de/DE/Vportal/TK/Funktechnik/EMF/start.html.

[18] Deutsche Telekom Technik GmbH, EMVU Umwelt und Nachhaltigkeit, *Mobilfunk und Gesundheit*, 2020.

[19] P. Tichavsky, C. Muravchik, and A. Nehorai, "Posterior Cramér-Rao bounds for discrete-time nonlinear filtering," *IEEE Transactions on Signal Processing*, vol. 46, no. 5, pp. 1386–1396, 1998.